communications materials

A Nature Portfolio journal

Article

https://doi.org/10.1038/s43246-025-01062-0

Insight into the Ehrlich–Schwoebel barrier via three-dimensional atomic force microscopy mapping of surface potentials on Au (111)

Check for updates

Bugrahan Guner[1], Mehmet Z. Baykara[2] & Omur E. Dagdeviren[1] ✉

Thin film growth is a critical process enabling modern applications ranging from electronic devices to advanced coatings. Among the parameters that govern thin film growth, the Ehrlich-Schwoebel barrier stands out with its tight control over interlayer transfer and, consequently, kinetics-dominated film morphology. Despite its importance, the precise measurement of the Ehrlich-Schwoebel barrier remains complicated, presenting a critical impediment to rational thin film design. Here, we provide an insight into the Ehrlich-Schwoebel barrier over monoatomic step edges on Au (111) surfaces via three-dimensional atomic force microscopy (3D-AFM) with sub-nanometer spatial precision, minimizing the need for empirical model assumptions or theoretical calculations. Our measurements provide a quantitative, real-space view of the complex potential energy and force landscape near step edges, verifying the presence of energy barriers and wells at the top and bottom of step edges, respectively. The effect of the herringbone reconstruction on the potential energy landscape is also analyzed, revealing an enhancement of interactions near the elbows and a slight attenuation of the ridges.

Solid thin films are of crucial importance from both fundamental and applied aspects. Modern electronic devices employ transistors relying on thin films[1], while thin-film-based solar cells[2] and thin film solid oxide fuel cells[3] are being intensely studied for sustainable energy applications. Thin film growth, broadly governed by energetic and kinetic factors, also plays a major role in the accelerating research area of two-dimensional (2D) materials, where methods based on chemical vapor deposition (CVD) are being used to grow films of graphene[4] and transition metal dichalcogenides down to monolayer thicknesses[5] on various substrates. On a more fundamental note, most emergent phenomena of interest in condensed matter are a direct result of dimensional reduction, whereby thin films of various materials are being actively investigated in areas, such as topological electronics, magnetics, and spintronics[6–8].

The scientific and technological importance posed by thin films warrants the formation of a detailed understanding of their growth mechanisms, which ultimately determine their structure (e.g., thickness and morphology) and consequently, their potential for implementation in devices as well as physicochemical characteristics including but not limited to chemical reactivity[9]. The basic idea behind this line of reasoning is that a complete understanding of growth mechanisms would enable the rational tuning of parameters to arrive at a desired set of structural characteristics. It has been known for multiple decades that thin film growth processes are governed by energetic and kinetic parameters. For film growth governed primarily by kinetics, typically far from thermodynamic equilibrium and occurring at lower temperatures, key factors include the interaction energies between adsorbates and substrate atoms, the atomic-scale morphology of the substrate, and the energy barriers that adsorbates must overcome during surface diffusion. Different parameters can result in distinctive kinetics-dominated growth modes: while weak adsorbate-substrate interactions (compared to interactions between adsorbate species) are typically associated with layer-by-layer growth and atomically smooth film surfaces, the inverse scenario generally results in nucleation and growth of individual islands, and consequently, a rough, *mounded* film morphology[10]. Equally importantly, the atomic-scale structure of the substrate surface plays a decisive role in thin film growth. In particular, Schwoebel, in 1966[11], theorized that atoms diffusing on a crystalline surface consisting of terraces and step edges would experience a higher energy barrier (compared to the diffusion energy barrier experienced on terraces) when moving *down* a step edge, to an underlying terrace. Conversely, when an atom attempts to move *up* a step edge, it enters a potential energy well at the bottom of the step, and a

---

[1]Department of Mechanical Engineering, École de technologie supérieure, University of Quebec, Montreal, QC, Canada. [2]Department of Mechanical Engineering, University of California Merced, Merced, CA, USA. ✉e-mail: omur.dagdeviren@etsmtl.ca

significantly larger energy barrier needs to be overcome for the atom to be able to move to the terrace above. The underlying reason for this additional energy barrier encountered at step edges (commonly referred to as the Ehrlich-Schwoebel barrier, due to complementary work by Ehrlich, published in 1966[12,13]) is the different coordination number exhibited by atoms at the top and bottom of step edges when compared to atoms on terraces. In particular, atoms on top of a step edge are *undercoordinated*, as they have fewer neighboring atoms than a regular atom on a terrace. Conversely, atoms at the bottom of a step edge are *overcoordinated*, featuring more neighboring atoms than a terrace atom. The earlier scenario leads to an enhanced energy barrier encountered by an adsorbate approaching the top of a step edge, whereas the latter scenario results in a pronounced potential energy well encountered by an adsorbate moving toward the bottom of a step edge. As the Ehrlich-Schwoebel barrier controls atomic-scale transport between layers during thin film growth, it plays a major role in kinetics-dominated growth. Specifically, high values of the Ehrlich-Schwoebel barrier restrict interlayer transfer, facilitating individual island growth, whereas relatively low values of the Ehrlich-Schwoebel barrier are typically needed for layer-by-layer growth.

Despite the importance of the Ehrlich-Schwoebel barrier for thin film growth, its determination remains complicated. While ab initio methods can be used to predict barrier heights for different materials[14,15], experimental attempts at the measurement of the Ehrlich-Schwoebel remain model-dependent, as they rely on the use of data provided by spectroscopic[16] or scanning probe microscopy (SPM)-based methods[17], in combination with theoretical growth models and/or computational approaches, such as Monte Carlo simulations[18,19]. The lack of assumption-free, model-independent measurements of the Ehrlich-Schwoebel barrier presents an important scientific hurdle, as experiments performed on the same material system can result in significantly different barrier heights depending on which theoretical model is employed to fit the data[20]. Experimental assessment of the potential energy variation across step edges with minimal assumptions is particularly important because electric-field-induced sub-picometer displacements of edge atoms can have pronounced effects, especially in ionic materials[21]. Even slight perturbations in the electrostatic interactions of these displaced ions can generate long-range variations in the potential energy landscape[21]. Moreover, the smoothing of electron charge at the step edges and corrugations, a.k.a. the Smoluchowski effect, modifies the charge distribution across step edges[22,23]. Nonetheless, such potential energy and force modifications induced by step edges can be directly probed using dynamic force microscopy measurements[24].

Motivated by these considerations, we present an experimental quantification of the local tip-sample potential modulation associated with the Ehrlich–Schwoebel barrier using three-dimensional atomic force microscopy (3D-AFM)[25–28] on the prototypical Au (111) surface with its characteristic herringbone reconstruction[29]. Using 3D maps of potential energies and forces acquired by gold-coated tips over monoatomic step edges, we verify the presence of and quantitatively analyze energy barriers and wells at the top and bottom of step edges, respectively. The measured values of barrier height, on the order of a few tenths of eV, are in agreement with theoretical expectations. Previously, surface energy landscapes of Au (111) were inferred from electron density maps using combined experimental and theoretical approaches, often relying on model-based screening[30]. In contrast, our method provides a complementary route by experimentally measuring spatially resolved potential energy and force fields, without invoking electron density-based models. Specifically, we map the potential energy landscape across the reconstructed Au (111) surface, including ridges and elbow sites of the herringbone structure, thereby revealing quantitative variations in local interaction relevant to surface-mediated processes[31].

Results

Three-dimensional mapping of interaction energy and forces at step-edges

In order to validate the existence of and quantitatively approximate the Ehrlich-Schwoebel barrier, we performed 3D-AFM measurements on a $14.2 \times 17.7\ \text{nm}^2$ region of the Au (111) surface that contains a monoatomic step edge (please see Methods for details of sample preparation and measurements)[32,33]. Briefly, to obtain spatially-resolved tip-sample interaction energies, $U_{tip\text{--}sample}(x, y, z)$, we performed 3D-AFM measurements as illustrated in Fig. 1. Multipass frequency-shift maps were recorded at 41 vertical positions at a constant closest tip-sample separation (d, different than the piezo position, z) as shown in Fig. 1a, with denser sampling closer to

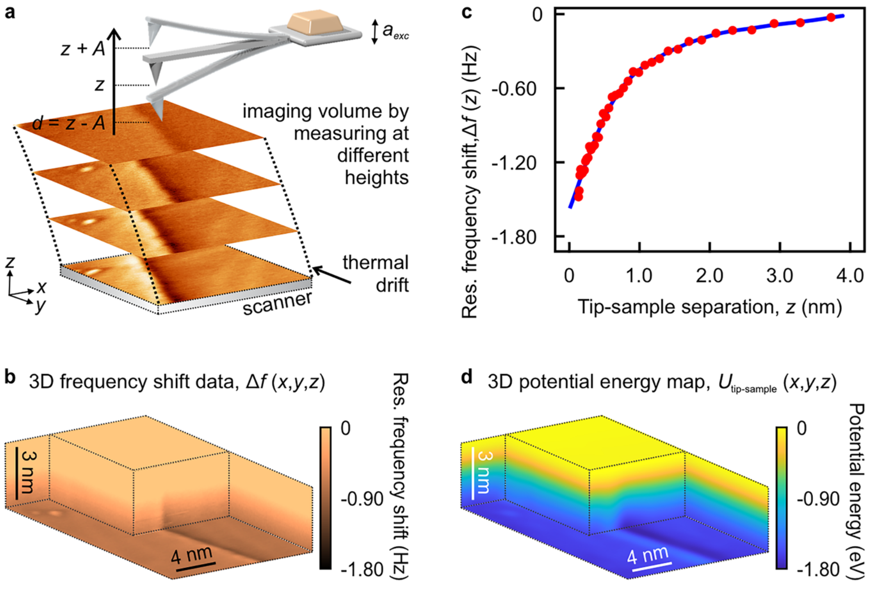

Fig. 1 | Schematic description of AFM measurements to access 3D tip-sample interaction energy data, $U_{\text{tip-sample}}(x, y, z)$. **a** Multipass measurements were performed at 41 different vertical distances z, the spacing of which was adjusted to maximize data density closer to the sample. The data are presented as a function of the closest tip-sample distance, d, which was calculated by employing the undeflected beam position and the reference scan recorded with constant current mode as the reference (see Methods section for details). Note that d is different than the piezo position, z. The oscillation amplitude, A, was kept constant by adjusting the excitation signal, a_{exc}. **b** The deflection signal of the oscillating sensor was demodulated as a function of the spatial position, delivering frequency shift data, $\Delta f(x, y, z)$. **c** For each lateral position (i.e., x and y coordinate), $\Delta f(z)$ data were used for numerical interpolation with 512 points as a function of tip-sample separation. **d** The resulting numerical fit of $\Delta f(z)$ for each lateral coordinate was employed to reconstruct $U_{\text{tip-sample}}(x, y, z)$. The calculation of $U_{\text{tip-sample}}(x, y, z)$ enables access to the tip-sample interaction force, $F_{\text{tip-sample}}(x, y, z)$, which was calculated via the negative partial derivative of $U_{\text{tip-sample}}(x, y, z)$ in each spatial direction. The data presented in this figure were recorded with an etched tungsten tip attached to the end of a qPlus sensor, on an atomically clean Au (111) sample.

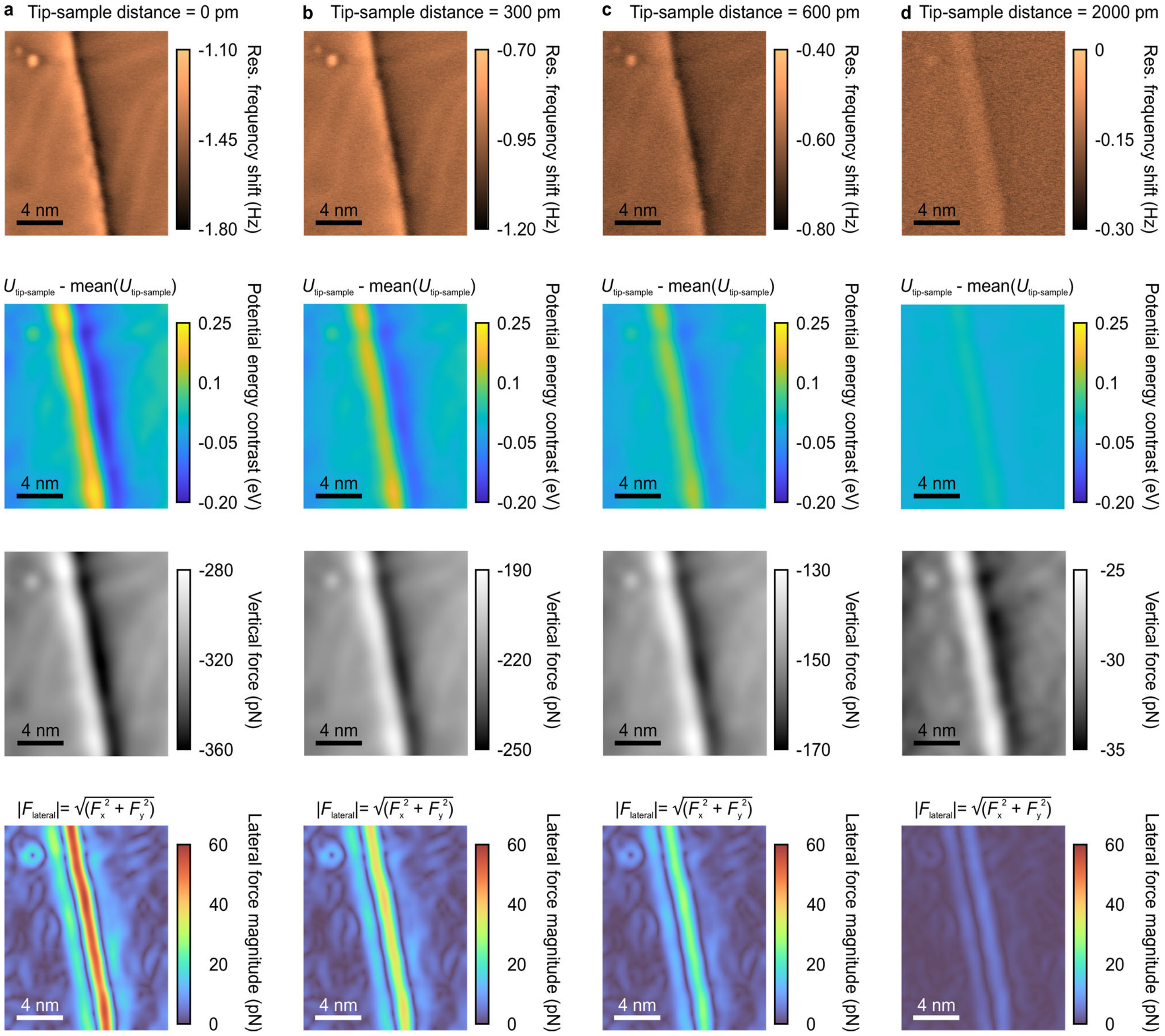

Fig. 2 | 3D-AFM measurements near a monoatomic step edge on the Au (111) surface. (x, y) maps of frequency shift (Δf, first row), potential energy contrast ($U_{\text{tip-sample}} - \text{mean}(U_{\text{tip-sample}})$, second row), vertical force (F_z, third row), and absolute lateral force ($\sqrt{F_x^2 + F_y^2}$, fourth row) acquired at four different tip-sample distances (**a** 0, **b** 300, **c** 600, and **d** 2000 pm).

the surface to enhance data resolution[34,35]. Figure 1b, c illustrate that the oscillating sensor's deflection signal was demodulated to yield $\Delta f(x, y, z)$ data, which were numerically interpolated for each lateral coordinate (*x,y*) and for each *d*. As shown in Fig. 1c, d, these interpolated $\Delta f(z)$ curves were then used to reconstruct $U_{tip--sample}(x, y, z)$, from which the corresponding interaction forces, $F_{tip--sample}(x, y, z)$, were obtained via spatial differentiation along lateral directions (*x,y*) and along vertical direction (presented by the closest tip-sample separation, see Methods for details). These potential energy and force maps are mathematically reconstructed from the experimentally acquired frequency shift data using established inversion techniques, particularly compatible with well-posed measurements[36,37]. Crucially, the reconstruction process does not rely on any system-dependent assumptions, diffusion rate models, or atomistic simulations, enabling an approximate quantification of the Ehrlich-Schwoebel barrier with sub-nanometer spatial precision.

Experimental visualization of the step-edge-induced potential energy variation

Representative (x, y) maps of frequency shift (Δf), potential energy contrast ($U_{\text{tip-sample}} - \text{mean}(U_{\text{tip-sample}})$), vertical force ($F_z$), and absolute lateral force ($\sqrt{F_x^2 + F_y^2}$) acquired at four different tip-sample distances (0, 300, 600, and 2000 pm (please see Supplementary Video 1 for details of lateral force, F_x), whereby 0 has been assigned to the closest tip-sample distance probed during the measurements) are presented in Fig. 2 (please see Supplementary Videos 1–5 for further details). One can clearly observe the step edge in Δf maps separating two terraces (upper terrace on the left, lower terrace on the right). Both terraces feature the characteristic ridges associated with the herringbone reconstruction, whereby an "elbow" is located near the lower left corner of the images, highlighted by enhanced frequency shift detectable as a "dark" spot. The area also features two adsorbates near the upper left corner, highlighted by attenuated frequency shift in the form of two "bright" spots. As the tip-sample distance increases from 0 to 2000 pm, both the average frequency shift (from -1.42 to -0.16 Hz) and the frequency shift contrast (from 0.67 to 0.21 Hz) change appreciably, whereby the existence of the herringbone ridges and elbow are not detectable anymore at the largest distance. The latter observation suggests that short-range rather than long-range interactions (e.g., van der Waals and electrostatic) are responsible for contrast formation in these measurements conducted by gold-coated tips on gold surfaces. A main advantage of the 3D-AFM methodology is the fact

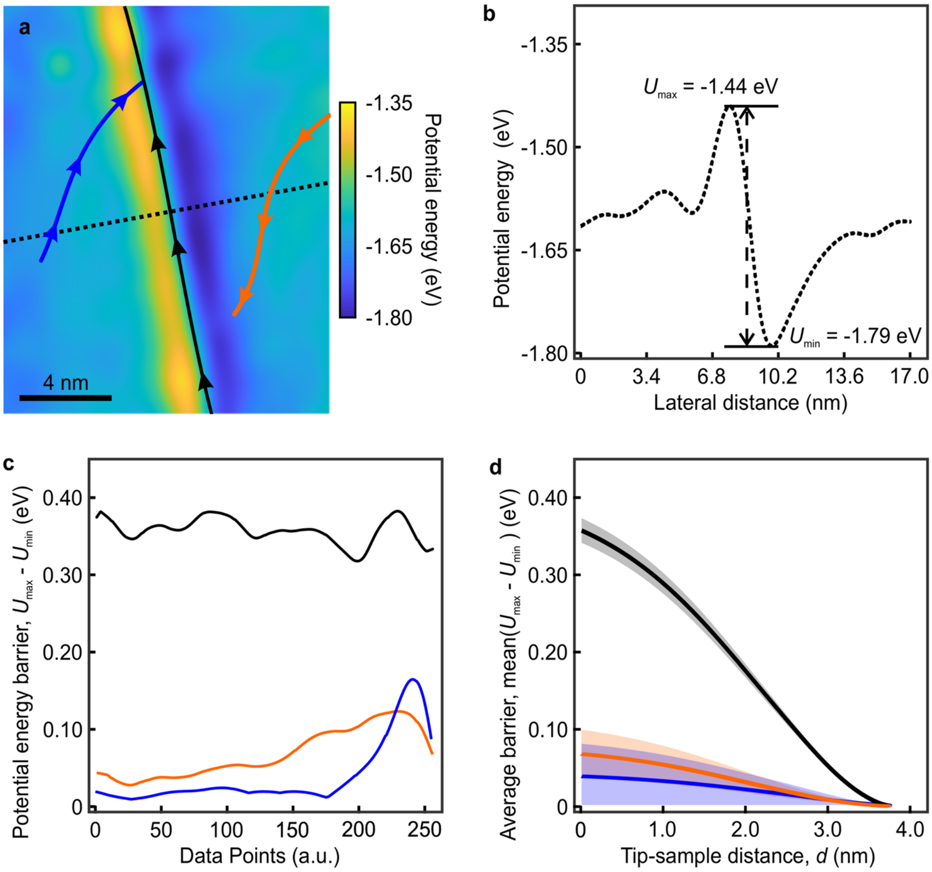

Fig. 3 | Quantitative evaluation of local potential energy variations on the Au (111) surface. a The $U_{\text{tip-sample}}$ map at the closest tip-sample distance ($d = 0$ nm), where the black line with arrows runs along the step edge, and the blue and orange lines with arrows run along herringbone ridges on the top and bottom terraces, respectively. **b** Plot of potential energy as a function of lateral position along the dashed black line shown in (**a**). The line profile clearly shows the presence of an energy barrier at the top of the step edge and an energy well at the bottom of the step edge. The total energy contrast between the top of the barrier and the bottom of the well near the step edge ($U_{max} - U_{min}$) is ~350 meV. **c** Plot of ($U_{max} - U_{min}$) values measured across the black, blue, and orange lines in (**a**), moving along the directions shown with arrows over 256 equally spaced data points. **d** The evolution of ($U_{max} - U_{min}$) values measured along the black, blue, and orange lines in (**a**) as a function of tip-sample distance, i.e., profiles similar to the ones presented in (**c**), was analyzed as a function of tip-sample distance. The solid lines show average values, whereas the shaded areas show the variation at each tip-sample distance.

that tip-sample interactions captured via frequency shift data are converted to (physically more meaningful) interaction energy and force values. Remarkably, the potential energy contrast maps presented in Fig. 2 confirm the presence of the Ehrlich-Schwoebel barrier on top of the monoatomic step edge, approximated in the form of a bright yellow band, i.e., a spatially-dependent potential energy variation across the step edge. By way of data acquired at the closest tip-sample distance, one can see that the potential energy increases by ~150 ± 20 meV on the upper terrace near the step edge, compared to values encountered away from the step edge. In a complementary fashion, the measurements also reveal the presence of an extended potential energy well (in the form of a dark blue band running along the bottom of the step edge). The potential energy locally reduces by ~200 ± 20 meV in the band, compared to the energy encountered away from the step edge on the lower terrace. As expected, increasing the tip-sample separation leads to a reduction in the overall potential energy contrast (from 370 to 50 meV), and the influence of the Ehrlich-Schwoebel barrier is barely detectable at the largest separation. Distance-dependent vertical force data presented in Fig. 2 reinforce the conclusions of the potential energy analysis, with the tip experiencing significantly enhanced attractive forces at the bottom of the step edge compared to the top (mean values of −355 ± 4 vs. −288 ± 5 pN). Vertical force maps, which again diminish in contrast with increasing tip-sample distance, also reveal the influence of the herringbone reconstruction and adsorbates on tip-sample interactions. In particular, while herringbone ridges and adsorbates locally attenuate the attractive interaction, a distinct enhancement of attraction (by ~25 pN, at the closest tip-sample separation) is detected at the herringbone elbow near the lower left corner of the map. Finally, maps of absolute lateral force presented in Fig. 2 highlight the effect of step edges on atoms in close proximity to them. Specifically, lateral forces are enhanced in magnitude near the step edges, whereby the lateral forces experienced by the AFM tip near the bottom of the step edge (~54 ± 4 pN, at $d = 0$) are noticeably higher than lateral forces experienced near the top of the step edge (~24 ± 2 pN, at $d = 0$). Intricate patterns of lateral forces, induced by the herringbone reconstruction and adsorbates, are additionally detected on both terraces; however, some finer details are blurred in the absolute lateral force maps. For a clearer visualization, we refer the reader to Supplementary Video 1, which distinguishes the absolute lateral force from the component along the scan direction, i.e., F_x. The overall contrast in the lateral force maps diminishes with increasing tip-sample distance (from 57 to 7 pN), as is the case for the other maps presented in Fig. 2.

Distance dependence and spatial heterogeneity of the energy landscape

Data presented in Fig. 3 allows a more detailed study of potential energy variations induced by the step edge and the herringbone reconstruction on the Au (111) surface. Focusing on the potential energy map recorded at the closest tip-sample distance (Fig. 3a), the representative profile in Fig. 3b demonstrates a striking resemblance to theoretical expectations by Schwoebel[11], quantitatively describing how the potential energy increases on top of the step edge in the form of a barrier and how the potential energy locally reaches a minimum at the bottom of the step edge, with a total drop in energy of ~350 meV from the top to the bottom of the step edge. Going into more detail, the data presented in Fig. 3c show how the total change in energy near the step edge, including kink sites, evolves as a function of position on the step edge, showing a mean value of 350 ± 20 meV with fluctuations on the order of 5% and below. While the physical reason behind these fluctuations is not trivially deducible from the data, small molecular adsorbates and/or atomic-scale changes in the structure of the step edge constitute potential mechanisms. Energy variations induced by herringbone ridges are also analyzed by way of profiles presented in Fig. 3c. Moreover, plotting the energy change along line profiles (shown in Fig. 3a) as a function of tip-sample distance reveals a gradual decrease of mean tip-sample potential energy, with the contrast becoming undetectable after d values larger than ~3.5 nm, as presented in Fig. 3d. The changes in potential energy induced by the herringbone ridges are detectable, although they are at least 80% lower compared to energy changes induced by the step edge. In regions where ridges get close to step edges, the energy landscape is dominated by the barriers and wells near the step edge. Similar to the energy contrast at step edges, the contrast on the herringbone ridges becomes weaker with increasing tip-sample distance, becoming undetectable after d values larger than ~3 nm.

Lateral and vertical force signatures of the Ehrlich–Schwoebel barrier

The potential energy landscape and the forces that are expected to be experienced by an adsorbed atom near the step edge are approximated with the help of (x, z) maps presented in Fig. 4. More specifically, dynamic scanning tunneling spectroscopy measurements reveal that the equilibrium position of the tip–sample interaction potential is approximately 0.07 nm closer than the closest experimentally accessible tip–sample distance (i.e., $d = 0$ nm; see Fig. S1). Although, in the strict sense, the Ehrlich-Schwoebel barrier corresponds to the energy that an adsorbate atom must overcome at this equilibrium separation, direct measurement of the potential energy landscape at smaller distances was not feasible. At smaller tip-sample separations, the Au-terminated tip engages in strong interactions with the surface, resulting in irreversible modifications of both the tip and the sample. While atomically engineered probes, such as CO-terminated tips, could, in principle, permit measurements at closer distances owing to their chemical inertness, such approaches would be compromised by the low lateral stiffness of the molecular apex[38–40] and its heterogeneous interaction with the surface Au atoms. As expected, the magnitude of the potential energy (Fig. 4a), as well as the total interaction force (Fig. 4b), increases monotonically with decreasing tip-sample distance, whereby the vertical force component (Fig. 4c) is always attractive, and its magnitude is at a minimum (maximum) at the top (bottom) of the step edge. The lateral force (x, z) map (Fig. 4d) is somewhat more complex. As the tip approaches the step edge (i.e., moves towards the right) on the upper terrace, it experiences a repulsive lateral force (of peak magnitude 23 ± 3 pN) due to the presence of the Ehrlich-Schwoebel barrier. Dragging the tip across the step edge then results in a transient lateral force (of peak magnitude 53 ± 3 pN) in the opposite direction (i.e., towards the right), as the downward slope in the potential energy landscape is traversed. Moving the tip further away from the step edge on the lower terrace again leads to the recording of a lateral force towards the step edge (i.e., to the left, of peak magnitude 13 ± 3 pN), due to the presence of the potential energy well at the bottom of the step. This complex lateral force behavior indeed verifies what adsorbed species diffusing on stepped crystalline surfaces are expected to encounter in the vicinity of step edges based on the Ehrlich-Schwoebel theory (Fig. 4e, f)[11]. The presence of the Ehrlich-Schwoebel barrier leads to a repulsive force for adsorbates attempting to move to a lower terrace (and thus, frequent "reflections" from step edges), whereas the potential energy well at the bottom of the step edge causes adsorbates on the lower terrace to be "captured" when they move too close to the step edges.

Discussion

Our findings unequivocally point to the existence of the Ehrlich-Schwoebel barrier atop step edges, based on measured energy and force data obtained via 3D-AFM. An important follow-up question is whether the barrier heights we measure (150 ± 20 meV) are in agreement with expectations from the literature, obtained either by way of simulations or model-dependent measurements, via microscopy/spectroscopy experiments in conjunction with theoretical models. More specifically, previous experimental approaches have primarily relied on the interpretation of data through atomistic diffusion or nucleation models. Notably, focused ion beam microscopy-based measurements were first conducted by Ehrlich, who assessed diffusion rates along various crystallographic directions using atomistic frameworks[13]. Subsequent interlayer mass transport studies on metal surfaces, e.g., Ag on Ag (111) (interpreted via nucleation kinetics), reported Ehrlich-Schwoebel barrier values around 120 ± 15 meV for homoepitaxial systems[41]. Other epitaxial growth studies, also relying on diffusion models, yielded barriers of ~150 meV and ~165 meV for Ag (111) and Pt (111) surfaces, respectively[42]. Additionally, ripening-based estimates reported a value of 130 ± 40 meV for the Ag on Ag (111) system[43]. Perhaps the most direct effort toward quantifying the force required to move a single atom over a surface was reported by Ternes et al. [44]. Specifically, the work involved measuring lateral forces required to move a single Co atom or CO molecule over the Cu (111) surface; whereby integration of forces allowed the determination of the involved energy barriers. This technique offered fundamental insights into atomic diffusion on flat, periodic surfaces. More recently, dynamic STM measurements of Au island coarsening and decay on Au (111) surfaces have been reported, where the Ehrlich-Schwoebel barrier for Au on Au (111) has been estimated as ~110 meV[17]. On the other hand, theoretical analysis considering different transport mechanisms over steps (including hopping as well as atomic exchange) has yielded barrier values between 160 and 180 meV[45,46]. Thus, it is clear that the barrier heights we directly measure via 3D-AFM using a gold-coated tip on Au (111) are in the same regime as estimated values in the literature. Most importantly, our approach enables spatially resolved measurement of interaction energies and forces over monoatomic step edges. By employing 3D-AFM, we avoid the need for atomistic diffusion or nucleation models and robustly reconstruct potential energy and force landscapes from experimentally measured frequency shifts, even in regions where surface symmetry is broken. This approach enables probing of the potential energy landscape across step edges, associated with the Ehrlich–Schwoebel barrier, under conditions relevant to non-equilibrium thin film growth, i.e., epitaxial growth[47], providing insights into the local energy landscape while representing a reasonable proxy for the actual adatom diffusion barrier.

Another important question regarding our experiments revolves around the tip-sample distance at which we conduct our measurements. This question arises naturally when one considers that the Ehrlich-Schwoebel barrier is originally defined for adsorbed atoms diffusing on surfaces, whereas our AFM tip is also in close proximity to the surface, but continuously in the attractive regime of interactions. The clear observation of the energy barrier (well) at the top (bottom) of step edges, combined with the quantitative agreement between measured barrier heights and those estimated in the literature, reinforces the idea that our closest tip-sample distance is indeed relevant for accurate measurements of the Ehrlich-Schwoebel barrier. Moreover, the barrier contrast plot shown in Fig. 3d appears to be reaching a saturation point as the tip-sample distance gets smaller. To support these arguments, we performed force and tunneling current spectroscopy experiments with our gold-coated tips on the Au (111) surface (Fig. S1), allowing us to estimate an effective closest tip-sample distance of ~0.07 nm for our measurements. Last but not least, to answer the question of whether our tips are indeed terminated by gold atoms, we performed tunneling spectroscopy experiments on the Au (111) surface (Fig. S2), the results of which are in agreement with expectations from gold tips.

An important observation from our experiments is that the effect of the energy well at the bottom of the step edges on the overall energy landscape is somewhat stronger than the energy barrier encountered at the top of the step edge (~200 meV vs. ~150 meV, respectively). This observation is in agreement with the original work by Schwoebel, where the energy well is sketched to be more pronounced than the barrier[11], implying that the degree of undercoordination experienced by an adsorbed atom approaching the step edge on the upper terrace is somewhat lower than the degree of overcoordination experienced by an atom approaching the step edge on the lower terrace.

Despite its inertness against environmental degradation in macroscopic form, gold has been found to be a particularly relevant catalyst for several chemical reactions (including but not limited to the oxidation of molecules, such as CO and CH_4) when deployed on smaller length scales, featuring high selectivity and reactivity at relatively low temperatures[48]. In heterogeneous catalysis, the formation of a local understanding of interaction is crucial for effective catalyst design, with full consideration of surface

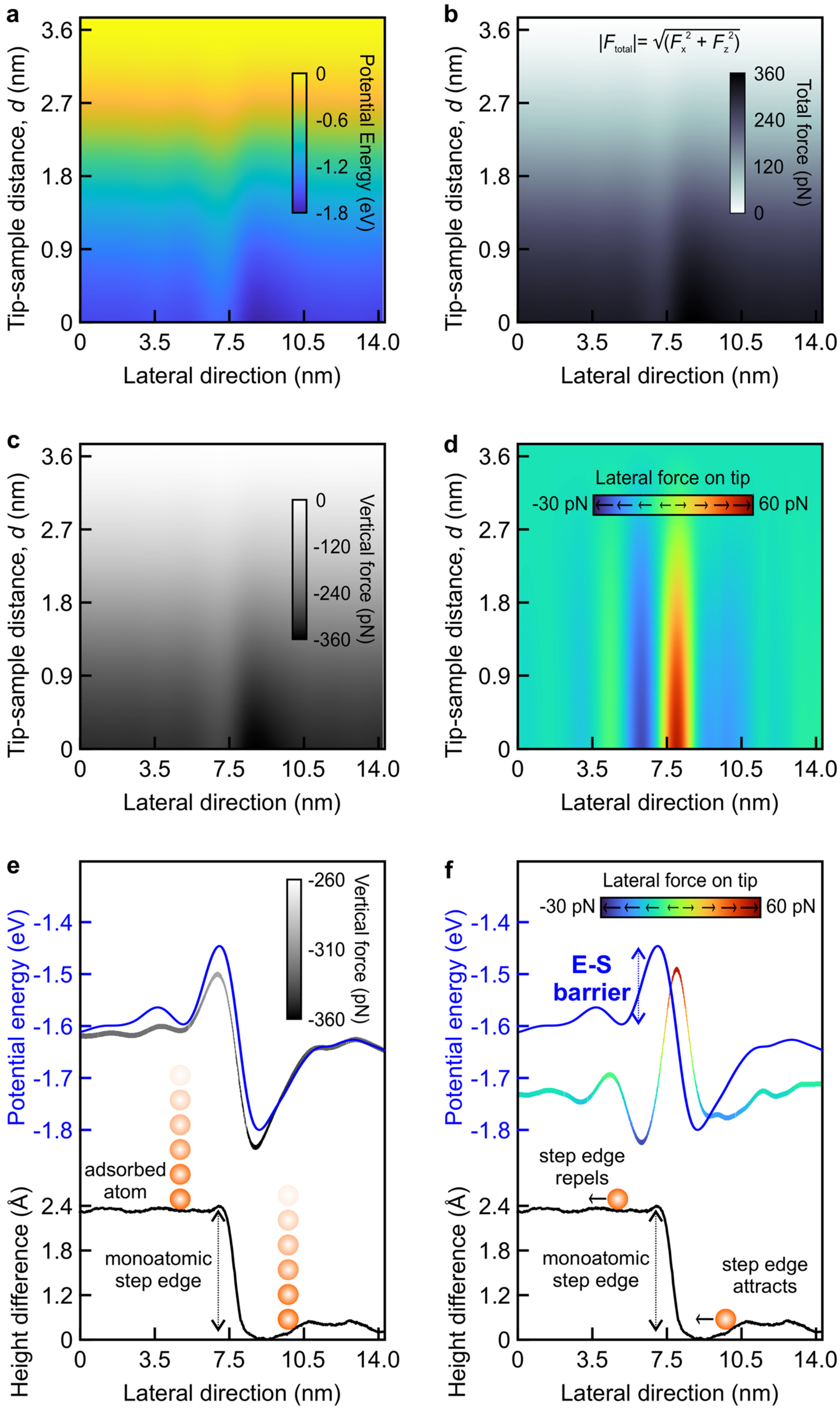

Fig. 4 | Potential energy and force as a function of tip-sample distance near a monoatomic step edge on the Au (111) surface. (x, z) maps of (**a**) potential energy, (**b**) total force, (**c**) vertical force, and (**d**) lateral force. **e** Profiles of potential energy and vertical force experienced by the tip around the step edge at the closest tip-sample distance, together with the topography of the region around the step edge where representative adsorbed atoms on upper and lower terraces are illustrated. **f** Profiles of potential energy and lateral force experienced by the tip around the step edge at the closest tip-sample distance, together with the topography of the region around the step edge, where the lateral forces experienced by representative adsorbed atoms on the upper and lower terraces are illustrated. The colormap presented in (**b**, bone scale) is different than the colormap in (**c**) and Fig. 2 (gray scale).

defects including but not limited to step edges and dislocations, which are often thought to be "hot spots" for chemical reactions due to their favorably modified energetics when compared with defect-free surface regions. Within this context, the (111) surface of gold presents a particularly interesting case thanks to the herringbone reconstruction[29]. While DFT calculations have predicted that adsorption energies at elbow locations are higher (indicating stronger adsorption) when compared with non-defective locations[49], and our scanning tunneling microscopy (STM) imaging experiments reveal preferential adsorption and long dwell times of CO molecules at elbows (see Fig. S3), no direct experimental quantification of interaction energy was so far performed on Au (111) surfaces. Results presented here indeed show enhanced chemical interaction with smaller potential energy landscapes at elbow locations, whereby modulations of ~70 meV are induced at the elbow sites compared to the surrounding region (please see Fig. 2, and the Supplementary Videos 1–4 for further details), a value on the same order of magnitude as expected from DFT studies of CO adsorption on the Au (111) surface[49,50]. Within this context, it is also interesting that potential energies are increased on the herringbone ridges (by ~30 meV), indicating a slightly lower chemical interaction. This may be caused by the increased atomic density on the surface induced by the herringbone reconstruction, resulting in a slight overcoordination (in contrast to Au atoms in the vicinity of elbow/dislocations which are undercoordinated and are thus expected to be chemically more active)[29].

Our methodology is not restricted to a single measurement on the Au (111) surface (see Fig. S4 and related text for additional data) and can be employed to study Ehrlich-Schwoebel barriers on other sample surfaces (as exemplified by data acquired on the highly oriented pyrolytic graphite (HOPG) (0001) surface; see Fig. S5), irrespective of electrical conductivity. Nevertheless, it is expected that different tip geometries can lead to different adsorption energies[51]. As shown in Fig. S4, measurements performed with different tip apexes, each consisting of an Au atom protruding from distinct Au clusters (resulting in different coordination numbers of the foremost Au atom), prepared by dipping the tip into Au (111) prior to 3D-AFM measurements, yield consistent results. Although the total tip–sample interaction potential can differ by up to ~50% for the same resonance frequency shift at the closest approach due to variations in the tip background, the ratio of the maximum-to-minimum interaction energy to the mean interaction energy varies by only about 2%, even across different atomic probes. This consistency demonstrates the reproducibility of the tip–sample interaction energy variation, an approximation to the Ehrlich-Schwoebel barrier, despite different Au cluster backgrounds of the tips. Likewise, the measured lateral forces are largely unaffected by variations in the atomic configuration of the tip apex. One should note that by using atomically engineered tips[38–40], e.g., CO-terminated tips, changes in the local energy landscape, including the Ehrlich–Schwoebel barrier, can be mapped at closer tip–sample separations due to their chemical inertness. However, the low lateral stiffness of such atomically engineered tips must be considered; CO-terminated tips, in particular, exhibit very low bending stiffness[38–40], despite their effectiveness for molecular imaging on flat surfaces. Additionally, molecular deposition on step edges could, in principle, affect the Ehrlich–Schwoebel barrier, as it modifies the local environment and the coordination of atoms at the upper and lower terrace edges. Moreover, such measurements can provide insight not only for chemical effects but also on the smearing of electrons due to step edges, i.e., the Smoluchowski effect[22,23]. Nevertheless, these approaches provide a route toward a comprehensive understanding of how surface defects, including but not limited to step edges, influence reactivity toward selected molecular species by enabling spatially resolved measurements of interaction energies.

Conclusions

We experimentally quantify the local tip–sample potential modulation associated with the Ehrlich–Schwoebel barrier using three-dimensional atomic force microscopy (3D-AFM) on monoatomic steps of Au (111). Our results reveal an energy barrier of height ~150 meV on top, and a well of depth ~200 meV on the bottom of step edges. Our experiments also allowed a real-space, quantitative evaluation of the effect of the herringbone reconstruction on the chemical interaction of the Au (111) surface. In particular, elbow locations were found to enhance interaction while ridges exhibited attenuation, attributed to under- and overcoordination of surface Au atoms, respectively. Our methodology on Au(111) may allow mapping of Ehrlich–Schwoebel barriers and the local surface energy landscape with rigid, chemically identified tips, providing spatially resolved insights into how surface defects influence atom-specific tip-sample interaction. This paves the way for rational catalyst design grounded in experimentally accessible energy landscapes.

Methods

Preparation of the Au (111) Sample

We employed a commercially available sample in the form of a 200 nm thick Au (111) film grown on mica (supplied by Scienta Omicron GmbH). Films were cleaned under ultra-high vacuum conditions (base pressure 2×10^{-11} mbar) by performing multiple Ar^+ sputtering (duration = 20 min, emission voltage = 1 kV, emission current = 10 mA, and Argon pressure = 5×10^{-6} mbar) and annealing cycles (30 min at 600 K). The monoatomic steps and cleanliness of the sample was verified via SPM measurements (see Figure S2 and the detailed explanation below)[32,33].

Preparation of the HOPG (0001) Sample

We exfoliated a bulk sample of HOPG (supplied by NanoAndMore) under ambient conditions via adhesive tape. AFM-based topography measurements were performed to validate the quality of the exfoliated sample[52] and the cleanliness of the region that we employed for experiments presented in Fig. S5.

SPM Measurements

We performed scanning tunneling microscopy (STM) and non-contact atomic force microscopy (NC-AFM) measurements on a 200 nm-thick Au (111) film grown on mica (see above for the details of sample preparation) by employing a low-temperature (9 K), ultra-high vacuum (2×10^{-11} mbar) microscope (Infinity Lab, Scienta Omicron GmbH). As Fig. S2 shows, the molecular-level cleanliness of the sample surface was verified using STM-based topography imaging. In addition to ensuring the cleanliness of the Au (111) film, scanning tunneling measurements were used to develop and test an atomically sharp, stable, and Au-terminated tip apex. Specifically, a chemically etched tungsten wire (Scienta Omicron GmbH) was pulsed on the Au sample multiple times (e.g., $V_{\text{pulse}} = 5$ V, pulse duration = 30 ms) to eliminate the oxide layer induced by etching. We also dipped the pulsed tip gently into the surface (e.g., by 0.3 nm) while applying a tip-sample bias voltage (e.g., $V_{\text{bias}} = 3$ V) and retracting away from the sample within a few seconds until the tunneling current between the tip and the sample ($I_{\text{tunneling}}$) was below the noise limit. Due to the stochastic nature of the tip-termination process, pulsing and dipping cycles were repeated multiple times until a stable, Au-terminated, atomically sharp tip was obtained. The condition of the tip was verified by imaging the sample at different $I_{\text{tunneling}}$ and V_{bias} combinations and via tunneling spectroscopy measurements (see Fig. S2).

It is known[53,54] that a plethora of experimental approaches are available to access the imaging volume across the surface: layer-by-layer data acquisition at constant tip-sample separations[25,55,56], curve-by-curve data acquisition (with atom tracking)[57–61], curve-by-curve or line-by-line acquisition involving reference imaging for drift correction[38,62], and constant height measurements on planar areas with no feedback[28]. We performed frequency modulation (FM)-based NC-AFM measurements on the Au (111) film by performing multipass measurements at different closest tip-sample separations along the vertical axis[34,35,63]. A qPlus sensor[64] (resonance frequency $f_0 = 23{,}307.36$ Hz, quality factor $Q = 38{,}495$, and spring constant, $k_{\text{qPlus}} \approx 2000$ N/m) with an etched tungsten wire attached to its end (see above) was mechanically excited at its base with amplitude a_{exc}. In close proximity to the sample, tip-sample interactions result in a resonance frequency shift, Δf, which was demodulated with a phase-locked loop (PLL). The oscillation amplitude of the qPlus sensor, A (peak amplitude = 5.0 Å), was kept constant during the FM measurements by adjusting a_{exc} with the PLL. The measurement remains well-posed throughout the investigated tip–sample distance range due to the appropriate choice of oscillation amplitude[36,37]. We automated multipass FM-based mapping, $\Delta f(x, y)$, for 41 different vertical distances with a custom Python code. We started from the smallest tip-sample separation to minimize tip/sample change during successive measurements. Mapping $\Delta f(x, y)$ at different tip-sample separations provided Δf data in three spatial dimensions, $\Delta f(x, y, z)$. All experimental data are transformed to the closest tip-sample separation for data representation, tip-sample interaction potential energy reconstruction and force calculations[25,55,56]. More specifically, we lifted the tip with respect to a reference scan recorded with STM feedback. The vertical height difference (i.e., spacing) between successive scans was adjusted to keep the average Δf variation nearly constant across all images, resulting in a higher concentration of data at smaller z values. Most importantly, repeating the reference scans with the same parameters (tunneling set point at 200 pA with a 200 mV bias voltage applied between the tip and the sample, ~7 h/image with a single pass measurement) and the same tip-sample separation enabled drift correction while avoiding relative tip and/or sample modifications as a function of tip-sample interaction force[65]. Moreover, as STM is sensitive to tip-sample separation even under attractive tip-sample interaction forces[66–68], measuring the reference scan with STM enabled precise tracking of the non-planar scan area. Also, STM measurements are dominated by the foremost atom in the tip apex, particularly at small tip-sample bias voltages[68,69]. Therefore, measuring the reference scans with STM ensured tip stability over the course of each experimental set (~ 280 h for 41 different tip-sample separations). Thermal drift (~0.8 Å/hour along the x direction, ~0.1 Å/hour along the y direction) was largely compensated during the measurements by adjusting the lateral position of the recorded images. Any remaining influence of thermal drift on the data was corrected during post-processing by employing cross-correlation across images recorded at different heights. The lateral region common to all 41 images was employed for data analysis. For each lateral position (*i.e.*, x, y coordinate), we fitted a spline curve (avoiding unphysical curve fitting-based oscillations at the data margins, i.e., at small and large z) to the experimental $\Delta f(z)$ data (number of logarithmically spaced data points for fitting = 512, smoothing factor = 0.99). The fitted $\Delta f(z)$ data were employed to reconstruct tip-sample interaction energy, $U_{\text{tip-sample}}\ (x, y, z)$[70]. The tip-sample interaction force, $F_{\text{tip-sample}}\ (x, y, z)$, was calculated as the negative of the partial derivative of $U_{\text{tip-sample}}$ along each spatial direction. Prior to numerical derivation, we interpolated $U_{\text{tip-sample}}\ (x, y, \text{z})$ maps for each z with a spline curve (smoothing factor = 0.99) along x and y coordinates to reduce noise induced by numerical derivation.

Complementing the measurements performed on Au (111), we conducted 2D (i.e., (x, z) mapping) FM-based NC-AFM measurements on an HOPG (0001) sample under ambient conditions (see above for sample preparation) by employing a customized microscope (EnviroScope by Veeco)[52]. We used a commercial cantilever (PPP-NCHR by Nanosensors, i.e., highly doped silicon probes, $f_0 = 313{,}277$ Hz, $Q = 281$, $k_{\text{cantilever}} \approx 20.9$ N/m) oscillated at a peak amplitude of 5.0 nm. We conducted 85 sequential topography measurements along a line profile at different Δf set points (automated with Python integration) while utilizing active drift/creep correction along the lateral directions (x and y) by measuring on the same region for more than four hours before data acquisition. A vertical drift rate of 1.2 Å/min was detected during the experiments, the influence of which was corrected in post-processing. The measured 2D $\Delta f\ (x, z)$ data were used to reconstruct $U_{\text{tip-sample}}\ (x, z)$. Performing calculations in two dimensions, we undertook the same mathematical approach as in the analysis of the Au (111) data (see above).

Data availability

Any relevant data are available from the authors upon reasonable request.

Code availability

The suite of MATLAB codes developed for this study can be accessed from the authors, and the report of its use should cite this work.

Received: 13 August 2025; Accepted: 18 December 2025;

References

1. Zhang, S. Review of modern field effect transistor technologies for scaling. *J. Phys. Conf. Ser.* **1617**, 012054 (2020).
2. Chopra, K. L., Paulson, P. D. & Dutta, V. Thin-film solar cells: an overview. *Prog. Photovoltaics Res. Appl.* **12**, 69–92 (2004).
3. Zhang, J., Ricote, S., Hendriksen, P. V. & Chen, Y. Advanced materials for thin-film solid oxide fuel cells: recent progress and challenges in boosting the device performance at low temperatures. *Adv. Funct. Mater.* **32**, 2111205 (2022).
4. Amontree, J. et al. Reproducible graphene synthesis by oxygen-free chemical vapour deposition. *Nature* **630**, 636–642 (2024).
5. Zhang, Y. et al. Recent progress in CVD growth of 2D transition metal dichalcogenides and related heterostructures. *Adv. Mater.* **31**, 1901694 (2019).
6. He, Q. L. et al. Topological transitions induced by antiferromagnetism in a thin-film topological insulator. *Phys. Rev. Lett.* **121**, 096802 (2018).
7. Dohi, T., Reeve, R. M. & Kläui, M. Thin film skyrmionics. *Annu. Rev. Condens. Matter Phys.* **13**, 73–95 (2022).
8. Chen, S. et al. Recent progress on topological structures in ferroic thin films and heterostructures. *Adv. Mater.* **33**, 2000857 (2021).
9. Luo, B. et al. Unravelling crystal growth of nanoparticles. *Nat. Nanotechnol.* **18**, 589–595 (2023).
10. Kaiser, N. Review of the fundamentals of thin-film growth. *Appl. Opt.* **41**, 3053–3060 (2002).
11. Schwoebel, R. L. & Shipsey, E. J. Step motion on crystal surfaces. *J. Appl. Phys.* **37**, 3682–3686 (1966).
12. Ehrlich, G. Atomic displacements in one- and two-dimensional diffusion. *J. Chem. Phys.* **44**, 1050–1055 (1966).
13. Ehrlich, G. & Hudda, F. G. Atomic view of surface self-diffusion: tungsten on tungsten. *J. Chem. Phys.* **44**, 1039–1049 (1966).
14. Xiang, S. K. & Huang, H. Ab initio determination of Ehrlich–Schwoebel barriers on Cu{111}. *Appl. Phys. Lett.* **92**, 101923 (2008).
15. Yin, H. et al. First-principles study on the effect of alloying elements on the Ehrlich–Schwoebel barriers on Ag(111). *Chem. Phys. Lett.* **846**, 141329 (2024).
16. Headrick, R. L. et al. Coherent X-ray measurement of step-flow propagation during growth on polycrystalline thin film surfaces. *Nat. Commun.* **10**, 2638 (2019).
17. Spurgeon, P. M., Lai, K. C., Han, Y., Evans, J. W. & Thiel, P. A. Fundamentals of Au(111) surface dynamics: coarsening of two-dimensional au islands. *J. Phys. Chem. C.* **124**, 7492–7499 (2020).
18. Politi, P. & Villain, J. Ehrlich-Schwoebel instability in molecular-beam epitaxy: a minimal model. *Phys. Rev. B* **54**, 5114–5129 (1996).
19. Gianfrancesco, A. G., Tselev, A., Baddorf, A. P., Kalinin, S. V. & Vasudevan, R. K. The Ehrlich–Schwoebel barrier on an oxide surface: a combined Monte-Carlo and in situ scanning tunneling microscopy approach. *Nanotechnology* **26**, 455705 (2015).
20. Krug, J., Politi, P. & Michely, T. Island nucleation in the presence of step-edge barriers: theory and applications. *Phys. Rev. B* **61**, 14037–14046 (2000).
21. Kawai, S. et al. Measuring electric field induced subpicometer displacement of step edge ions. *Phys. Rev. Lett.* **109**, 146101 (2012).
22. Avouris, P., Lyo, I. W. & Molinàs-Mata, P. STM studies of the interaction of surface state electrons on metals with steps and adsorbates. *Chem. Phys. Lett.* **240**, 423–428 (1995).
23. Smoluchowski, R. Anisotropy of the electronic work function of metals. *Phys. Rev.* **60**, 661–674 (1941).
24. Pfeiffer, O., Bennewitz, R., Baratoff, A., Meyer, E. & Grütter, P. Lateral-force measurements in dynamic force microscopy. *Phys. Rev. B* **65**, 161403 (2002).
25. Albers, B. J. et al. Three-dimensional imaging of short-range chemical forces with picometre resolution. *Nat. Nano* **4**, 307–310 (2009).
26. Baykara, M. Z., Schwendemann, T. C., Altman, E. I. & Schwarz, U. D. Three-dimensional atomic force microscopy – taking surface imaging to the next level. *Adv. Mater.* **22**, 2838–2853 (2010).
27. Shen, B. et al. A single-molecule van der Waals compass. *Nature* **592**, 541–544 (2021).
28. Wang, X., Zahl, P., Wang, H., Altman, E. I. & Schwarz, U. D. How precisely can individual molecules be analyzed? A case study on locally quantifying forces and energies using scanning probe microscopy. *ACS Nano* **18**, 4495–4506 (2024).
29. Li, P. & Ding, F. Origin of the herringbone reconstruction of Au(111) surface at the atomic scale. *Sci. Adv.* **8**, eabq2900 (2022).

30. Bürgi, L., Brune, H. & Kern, K. Imaging of electron potential landscapes on Au(111). *Phys. Rev. Lett.* **89**, 176801 (2002).
31. Gong, J. Structure and surface chemistry of gold-based model catalysts. *Chem. Rev.* **112**, 2987–3054 (2012).
32. Barth, J. V., Brune, H., Ertl, G. & Behm, R. J. Scanning tunneling microscopy observations on the reconstructed Au(111) surface: atomic structure, long-range superstructure, rotational domains, and surface defects. *Phys. Rev. B* **42**, 9307–9318 (1990).
33. Sandy, A. R., Mochrie, S. G. J., Zehner, D. M., Huang, K. G. & Gibbs, D. Structure and phases of the Au(111) surface: X-ray-scattering measurements. *Phys. Rev. B* **43**, 4667–4687 (1991).
34. Moreno, C., Stetsovych, O., Shimizu, T. K. & Custance, O. Imaging three-dimensional surface objects with submolecular resolution by atomic force microscopy. *Nano Lett.* **15**, 2257–2262 (2015).
35. Martin-Jimenez, D. et al. Bond-level imaging of the 3D conformation of adsorbed organic molecules using atomic force microscopy with simultaneous tunneling feedback. *Phys. Rev. Lett.* **122**, 196101 (2019).
36. Sader, J. E., Hughes, B. D., Huber, F. & Giessibl, F. J. Interatomic force laws that evade dynamic measurement. *Nat. Nanotechnol.* **13**, 1088–1091 (2018).
37. Dagdeviren, O. E., Zhou, C., Altman, E. I. & Schwarz, U. D. Quantifying tip-sample interactions in vacuum using cantilever-based sensors: an analysis. *Phys. Rev. Appl.* **9**, 044040 (2018).
38. Gross, L., Mohn, F., Moll, N., Liljeroth, P. & Meyer, G. The chemical structure of a molecule resolved by atomic force microscopy. *Science* **325**, 1110–1114 (2009).
39. Mönig, H. et al. Submolecular imaging by noncontact atomic force microscopy with an oxygen atom rigidly connected to a metallic probe. *ACS Nano* **10**, 1201–1209 (2016).
40. Kawai, S. et al. Van der Waals interactions and the limits of isolated atom models at interfaces. *Nat. Commun.* **7**, 11559 (2016).
41. Bromann, K., Brune, H., Röder, H. & Kern, K. Interlayer mass transport in homoepitaxial and heteroepitaxial metal growth. *Phys. Rev. Lett.* **75**, 677–680 (1995).
42. Meyer, J. A., Vrijmoeth, J., van der Vegt, H. A., Vlieg, E. & Behm, R. J. Importance of the additional step-edge barrier in determining film morphology during epitaxial growth. *Phys. Rev. B* **51**, 14790–14793 (1995).
43. Morgenstern, K., Rosenfeld, G., Lægsgaard, E., Besenbacher, F. & Comsa, G. Measurement of energies controlling ripening and annealing on metal surfaces. *Phys. Rev. Lett.* **80**, 556–559 (1998).
44. Ternes, M., Lutz, C. P., Hirjibehedin, C. F., Giessibl, F. J. & Heinrich, A. J. The force needed to move an atom on a surface. *Science* **319**, 1066–1069 (2008).
45. Stoltze, P. Simulation of surface defects. *J. Phys. Condens. Matter* **6**, 9495 (1994).
46. Kim, S. Y., Lee, I.-H. & Jun, S. Transition-pathway models of atomic diffusion on fcc metal surfaces. II. Stepped surfaces. *Phys. Rev. B* **76**, 245408 (2007).
47. Le Lay, G. & Kern, R. Physical methods used for the characterization of modes of epitaxial growth from the vapor phase. *J. Cryst. Growth* **44**, 197–222 (1978).
48. Baker, T. A., Liu, X. & Friend, C. M. The mystery of gold's chemical activity: local bonding, morphology and reactivity of atomic oxygen. *Phys. Chem. Chem. Phys.* **13**, 34–46 (2011).
49. Wang, J. et al. Formation, migration, and reactivity of Au–CO complexes on gold surfaces. *J. Am. Chem. Soc.* **138**, 1518–1526 (2016).
50. Marek, G., Andreas, E. & Jürgen, H. CO adsorption on close-packed transition and noble metal surfaces: trends from ab initio calculations. *J. Phys. Condens. Matter* **16**, 1141 (2004).
51. Berger, R. K., Jeindl, A., Hörmann, L. & Hofmann, O. T. Role of adatoms for the adsorption of F4TCNQ on Au(111). *J. Phys. Chem. C.* **126**, 7718–7727 (2022).
52. Guner, B., Laflamme, S. & Dagdeviren, O. E. Customization of an atomic force microscope for multidimensional measurements under environmental conditions. *Rev. Sci. Instrum.* **94**, 063704 (2023).
53. Hölscher, H., Langkat, S. M., Schwarz, A. & Wiesendanger, R. Measurement of three-dimensional force fields with atomic resolution using dynamic force spectroscopy. *Appl. Phys. Lett.* **81**, 4428–4430 (2002).
54. Schwarz, A., Hölscher, H. & Langkat, S. M. & Wiesendanger, R. Three-dimensional force field spectroscopy. *AIP Conf. Proc.* **696**, 68–78 (2003).
55. Albers, B. J. et al. Combined low-temperature scanning tunneling/atomic force microscope for atomic resolution imaging and site-specific force spectroscopy. *Rev. Sci. Instrum.* **79**, 033704 (2008).
56. Boris, J. A. et al. Data acquisition and analysis procedures for high-resolution atomic force microscopy in three dimensions. *Nanotechnology* **20**, 264002 (2009).
57. Kawai, S., Glatzel, T., Koch, S., Baratoff, A. & Meyer, E. Interaction-induced atomic displacements revealed by drift-corrected dynamic force spectroscopy. *Phys. Rev. B* **83**, 035421 (2011).
58. Sugimoto, Y., Ueda, K., Abe, M. & Morita, S. Three-dimensional scanning force/tunneling spectroscopy at room temperature. *J. Phys. Condens. Matter* **24**, 084008 (2012).
59. Fremy, S. et al. Three-dimensional dynamic force spectroscopy measurements on KBr(001): atomic deformations at small tip–sample separations. *Nanotechnology* **23**, 055401 (2012).
60. Rahe, P. et al. Flexible drift-compensation system for precise 3D force mapping in severe drift environments. *Rev. Sci. Instrum.* **82**, 063704 (2011).
61. Pawlak, R., Kawai, S., Fremy, S., Glatzel, T. & Meyer, E. Atomic-scale mechanical properties of orientated C60 molecules revealed by noncontact atomic force microscopy. *ACS Nano* **5**, 6349–6354 (2011).
62. Mohn, F., Gross, L. & Meyer, G. Measuring the short-range force field above a single molecule with atomic resolution. *Appl. Phys. Lett.* **99**, 053106 (2011).
63. Albrecht, T. R., Grutter, P., Horne, D. & Rugar, D. Frequency modulation detection using high-Q cantilevers for enhanced force microscope sensitivity. *J. Appl. Phys.* **69**, 668–673 (1991).
64. Giessibl, F. J. The qPlus sensor, a powerful core for the atomic force microscope. *Rev. Sci. Instrum.* **90**, 011101 (2019).
65. Baykara, M. Z. et al. Probing three-dimensional surface force fields with atomic resolution: measurement strategies, limitations, and artifact reduction. *Beilstein J. Nanotechnol.* **3**, 637–650 (2012).
66. Mönig, H. et al. Understanding scanning tunneling microscopy contrast mechanisms on metal oxides: a case study. *ACS Nano* **7**, 10233–10244 (2013).
67. Güthner, P. Simultaneous imaging of Si(111) 7×7 with atomic resolution in scanning tunneling microscopy, atomic force microscopy, and atomic force microscopy noncontact mode. *J. Vac. Sci. Technol. B* **14**, 2428–2431 (1996).
68. Chen, C. J. *Introduction to Scanning Tunneling Microscopy*. (Oxford University Press, 1993).
69. Baykara, M. Z. et al. Atom-specific forces and defect identification on surface-oxidized Cu(100) with combined 3D-AFM and STM measurements. *Phys. Rev. B* **87**, 155414 (2013).
70. Sader, J. E. & Jarvis, S. P. Accurate formulas for interaction force and energy in frequency modulation force spectroscopy. *Appl. Phys. Lett.* **84**, 1801–1803 (2004).

Acknowledgements

This work was supported by Le Fonds de Recherche du Québec - Nature et Technologies, the Canada Economic Development Fund, and the Natural Sciences and Engineering Research Council of Canada. O.E.D. also gratefully acknowledges funds provided by the École de technologie supérieure, University of Quebec.

Author contributions

O.E.D. conceived the project. O.E.D. and M.Z.B. wrote the manuscript. O.E.D. and B.G. designed experiments. B.G. prepared the samples and performed the measurements. O.E.D. analyzed all data and prepared all figures with the help of B.G. All authors participated in the interpretation of the data.

Competing interests

The authors declare no competing interests.

Additional information

Supplementary information The online version contains supplementary material available at https://doi.org/10.1038/s43246-025-01062-0.

Correspondence and requests for materials should be addressed to Omur E. Dagdeviren.

Peer review information *Communications Materials* thanks Zechao Yang and the other, anonymous, reviewer(s) for their contribution to the peer review of this work.

Reprints and permissions information is available at http://www.nature.com/reprints

Publisher's note Springer Nature remains neutral with regard to jurisdictional claims in published maps and institutional affiliations.

Open Access This article is licensed under a Creative Commons Attribution-NonCommercial-NoDerivatives 4.0 International License, which permits any non-commercial use, sharing, distribution and reproduction in any medium or format, as long as you give appropriate credit to the original author(s) and the source, provide a link to the Creative Commons licence, and indicate if you modified the licensed material. You do not have permission under this licence to share adapted material derived from this article or parts of it. The images or other third party material in this article are included in the article's Creative Commons licence, unless indicated otherwise in a credit line to the material. If material is not included in the article's Creative Commons licence and your intended use is not permitted by statutory regulation or exceeds the permitted use, you will need to obtain permission directly from the copyright holder. To view a copy of this licence, visit http://creativecommons.org/licenses/by-nc-nd/4.0/.

© The Author(s) 2025